ISSN 0912-232X

PHOTOMEDICINE AND PHOTOBIOLOGY

Vol.42 2020

The Japanese Society for Photomedicine and Photobiology

Photomedicine and Photobiology
Vol.42

2020

The Japanese Society for Photomedicine and Photobiology
Foundednin 1978

Office : Depaetment of Dermatology, Kobe University Graduate School of Medicine,
7-5-1 Kusunoki-cho, Chuo-ku, Kobe, 650-0017, Japan.

CONTENTS

【Article】

Localizations of the highest occupied molecular orbital and guanine oxidation by UV-light and other oxidizers.

Masayuki Morikawa, Katsuhito Kino*, Taishu Kawada and Hiroshi Miyazawa

Kagawa School of Pharmaceutical Sciences, Tokushima Bunri University, 1314-1 Shido, Sanuki, Kagawa 769-2193, Japan

***Corresponding author:**

Katsuhito Kino
Kagawa School of Pharmaceutical Sciences, Tokushima Bunri University, 1314-1 Shido, Sanuki, Kagawa 769-2193, Japan
TEL: +81-87-899-7463
FAX: +81-87-894-0181.
E-mail: kkino@kph.bunri-u.ac.jp

ABSTRACT

Each DNA base in an organism is occasionally damaged by UV-light or other oxidizers. Guanine is the most easily damaged base, and contiguous guanine sites, such as GG, GGG, and GGGG, are more easily oxidized than single guanine. In this review, we describe how highest occupied molecular orbital (HOMO) localizations are involved in guanine oxidation. In double-stranded DNA, the 5' side of GG steps is more easily oxidized than the 3' side because the HOMO is localized at the 5' side of GG. In human telomeric quadruplex DNA, the HOMO is localized on the 5'-guanine and this 5'-guanine is oxidized. In contrast, tetrahymena and oxytricha telomeric quadruplex DNA are oxidized at their 3'-guanines. Based on the results of calculations, the oxidation of 3'-guanines is due to the likely presence of a 5'-capping cation and/or the dimeric structure.

Key words: Highest occupied molecular orbital (HOMO), Guanine oxidation, Double-stranded DNA, Quadruplex DNA

Introduction

DNA encodes genetic information through the sequence of the four DNA bases (guanine, adenine, cytosine, and thymine). Although DNA is a highly stable molecule, each DNA base is occasionally oxidized by an encounter with environmental agents, such as UV-light or free radicals (1-15). The oxidation potentials for guanine, adenine, cytosine, and thymine are 1.29, 1.42, 1.6, and 1.7 V, respectively (16). Guanine is thus the base most easily damaged by one-electron oxidation, and several oxidation products are known (1-15). If left uncorrected when the DNA is replicated, some guanine oxidation products would likely lead to a genetic mutation in the daughter DNA chain.

A guanine in contiguous guanine sequences, such as GG and GGG, have lower oxidation potentials than single guanine, and thus a contiguous guanine is more easily oxidized. Contiguous guanine sequences appear in many important genomic regions, such as telomeres and the promoter element of the proto-oncogene c-myc (17-22). Several experimental approaches indicate that the 5' side of contiguous GG sequences in double-stranded DNA is more easily oxidized than the 3' side (23-39). This common pattern of site-specific oxidations using various oxidizers (23-39) likely originates from the common chemical properties of DNA bases themselves, but not from the chemical properties of oxidizers. Therefore, DNA without oxidizers can be calculated.

This review focuses on the localization of the highest occupied molecular orbital (HOMO) of guanine, and guanine oxidations are discussed in relation to computational approaches.

Double-stranded DNA

As mentioned above, the 5' side of GG steps is more easily oxidized than the 3' side in double-stranded DNA (23-39). This site-specific guanine oxidation has been extensively investigated using computational approaches to explain the correlation between site-specific oxidation and double-stranded DNA structure.

Colson *et al.* calculated monomeric nucleobase pairs and showed that the Koopmans' theorem values (the HOMO energy of the neutral DNA base) closely resembled the experimental vertical ionization potentials (40). Sugiyama and Saito also calculated the HOMO of the stacked nucleobase pairs in double-stranded DNA (41). The calculated HOMO energies were: 7.75 eV (G), 7.28 eV (GG), 7.07 eV (GGG), and 6.98 eV (GGGG), and HOMO energies decreased with increasing numbers of stacked guanines (41). In addition, the HOMO energies of dinucleotide base pairs in double-stranded DNA were: 6.73 eV (GG), 7.00 eV (CG), 7.01 eV (GA), 7.06 eV

(AG), 7.12 eV (TG), 7.23 eV (GT), and 7.33 eV (GC). Of these dinucleotide base pairs, GG has the lowest HOMO energy. There are several reported examples showing experimentally that guanine in contiguous guanine sequences in double-stranded DNA is more easily oxidized than single guanine, consistent with HOMO energy calculations (42-50).

Interestingly, approximately 70% of the HOMO is localized on the 5'-G of GG in the double-stranded DNA model shown in Fig. 1 (26,41,51,52). There are several reports that the 5'-guanine in contiguous guanine sequences, such as GG and GGG, in double-stranded DNA is more easily oxidized than other guanines (15,23-28), and the calculated HOMO of GGGG is in agreement with experimental results (53).

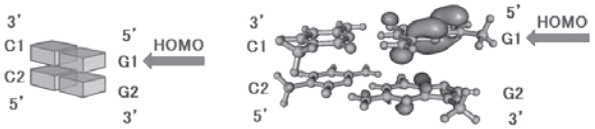

Fig. 1 HOMO localization on a 5'-G of GG step in double-stranded DNA. The geometry was constructed using Maestro 12.4 (Schrödinger), and all the sugar backbones were removed. The calculation of HOMO was performed at the B3LYP/6-31G* level utilizing Gaussian 03. The HOMO was visualized using Molekel 5.4.0.8.

Site-specific oxidation thus depends on the localization of the HOMO and can be explained as follows. Since the HOMO is localized at the 5'-guanine of stacked GG in double-stranded DNA, the 5'-guanine is the most electron-donating site (26,41,51,52), allowing its facile oxidation to a guanine radical cation ($G^{\bullet+}$). Several oxidation products can be formed from $G^{\bullet+}$ (1-15). The above-described localization of HOMO is consistent with experimental results for guanine oxidation in double-stranded DNA. Several other computational properties also are consistent with computational approaches using HOMO localization (29-39,54-59).

The localization of HOMO is likely induced by the geometries of stacked base pairs in double-stranded DNA. The HOMOs of stacked GGs with different twist angles were calculated (41). Typical twist angles for B-form DNA are between -45° and -25° and in this range, the HOMO is predominantly localized on the 5'-guanine. When the range of twist angles is between -25° and -18°, the HOMO is also predominantly localized on the 5'-guanine. In contrast, the HOMO is distributed equally on the two guanines when the range is between -18° and 18°. If the twist angle is above 18°, the HOMO is localized on the 3'-guanine.

N7 of the 3'-guanine is located just below the six-membered ring of the 5'- guanine in B-form double-stranded DNA (Fig. 2a) and thus the negative charge stabilizes a cation located in the 5'-guanine of a GG stack. Foote *et al*. proposed that this negative charge results in localization of the HOMO (60).

The HOMO localization of GG with complementary bases in A-form double-stranded DNA was calculated (41) and provided HOMO localizations very similar to that of the B-form double-stranded geometry. In A-form double-stranded DNA, N7 of the 3'-guanine is also located directly below the six-membered ring of the 5'-guanine, as in B-form double-stranded DNA. These similar geometries likely contribute to the observed nearly identical HOMO localizations in A-form and B-form double-stranded DNA.

Taken together, these results show that the distribution of HOMO largely depends on the stacking geometries of bases, suggesting that guanine oxidation in other DNA structures likely differs from that in double-stranded DNA due to differences in geometry.

Quadruplex DNA

As described above, guanine in contiguous guanine sequences is easily oxidized. Guanine-rich sequences can fold into quadruplex structures in the presence of metal cations (17-20). This section describes the influence of quadruplex structures on the reactivity of guanine.

Human telomeric quadruplex DNA ($d(TAGGGT)_4T$) was oxidized and the products identified (61). Oxidation occurred mainly on the 5'-guanines, consistent with experimental results obtained for double-stranded DNA (61). N7 of the 3'-guanine in ($d(TAGGGT)_4T$) is located below the six-membered ring of the 5'-guanine (Fig. 2b), similar to double-stranded DNA (Fig. 2a). HOMO localization of quadruplex DNA containing two potassium ions ($d(TAGGGT)_4T+2K^+$) was calculated at the B3LYP/6-31G* level and showed that the HOMO is predominantly localized on the 5'-guanine (61,62), compatible with the observed experimental selectivity in quadruplex DNA ($d(TAGGGT)_4T$). Similarly, a guanine-rich region of the *NEIL3* promoter can form a quadruplex structure, and the 5'-guanines and the unfolded guanines in the loop regions oxidize preferentially (63).

In contrast, experiments showed that tetrahymena and oxytricha telomeric quadruplex DNA ($d(TGGGGT)_4$) are oxidized at the 3'-guanine (64). The HOMO localization of $d(TGGGGT)_4+3K^+$ was determined computationally (PDB: 1S45) and found to mainly localize in the 5'-guanine (Fig. 3a), in contrast to the observed experimental data.

The reported crystallographic structures of $d(TGGGGT)_4$ (PDB: 1S45, 2GW0, and 204F) all have

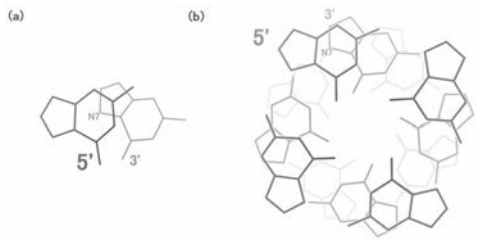

Fig. 2 Top view of arranged DNA with two stacked guanines: 5' (black, top), 3' (gray, bottom). N7 of the 3'-guanine is located just below the six-membered ring of the 5'- guanine in (a) B-form double-stranded DNA and (b) quadruplex DNA.

a “5’-capping” cation. Calculations were thus conducted for d(TGGGGT)$_4$+4K$^+$ (Fig. 3b), which has a 5’-capping cation attached to d(TGGGGT)$_4$+3K$^+$ (Fig. 3a) (62). Interestingly, the HOMO shifted from the 5’-guanine to the 3’-guanine (Fig. 3), explaining the observed experimental data.

Negative mode electrospray ionization-mass spectrometry (ESI-MS) of d(TGGGGT)$_4$ provided a main peak corresponding to d(TGGGGT)$_4$+3K$^+$. The relative intensities of this main peak to other ions were 0.81 for d(TGGGGT)$_4$+4K$^+$, 0.29 for d(TGGGGT)$_4$+5K$^+$, and 0.18 for d(TGGGGT)$_4$+6K$^+$ (64). Intensity decreases of these peaks at a constant rate should provide a relative intensity for d(TGGGGT)$_4$+4K$^+$ of 0.55 instead of 0.81. Therefore, d(TGGGGT)$_4$+4K$^+$ has a prominent peak height, suggesting the presence of d(TGGGGT)$_4$+4K$^+$. Assuming that d(TGGGGT)$_4$+4K$^+$ is the main product, the calculation result is in agreement with the experimental result. However, the applied high voltage and/or heated inert dry gas used in ESI-MS appears to convert d(TGGGGT)$_4$+4K$^+$ to d(TGGGGT)$_4$+3K$^+$. Taken together, these results indicate that HOMO localization depends on both the DNA stacking geometry and the locations and number of metal ion cations.

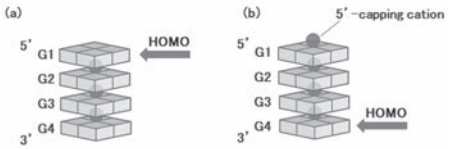

Fig. 3 The HOMO localization of d(TGGGGT)$_4$. The G-quartet plane and cations are shown as squares and circles. (a) d(TGGGGT)$_4$+3K$^+$ model. (b) d(TGGGGT)$_4$+4K$^+$ model; The 5’-capping cation is attached to the d(TGGGGT)$_4$+3K$^+$ model.

The influence of cations on HOMO localization was determined by removing one cation from d(TGGGGT)$_4$+4K$^+$ and calculating the HOMO (62). The first, second, third, and fourth G-quartet planes from the 5’-end were defined as the G1, G2, G3, and G4 planes, respectively. When a cation between the G3 and G4 planes was removed, the HOMO was located at the G4 plane (Fig. 4a). Figure 4b shows that the HOMO shifted at the G3 plane in the quadruplex structure when there was no cation between the G3 and G2 planes. Figure 4c shows that the HOMO was shifted at the G2 plane in the quadruplex structure lacking a cation between the G2 and G1 planes. Similarly, when two or three cations were removed, the HOMO shifted to the G-quartet plane lacking

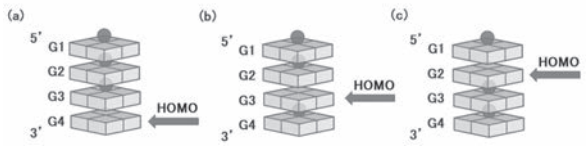

Fig. 4 The influence of cations on the HOMO. The G-quartet plane and cations are shown as squares and circles. One cation has been removed between (a) G3 and G4, (b) G2 and G3, (c) G1 and G2.

both neighboring cations (62). Collectively, localization of the HOMO at the G-quartet plane located immediately adjacent to the cation is generally disfavored.

Crystallographic data (PDB: 1S45, 2GW0, and 2O4F) support the dimeric structure and formation of the dimeric quadruplex structure (d(TGGGGT)$_8$ + 7K$^+$) was proposed (14). The 5’-capping cation may attach to d(TGGGGT)$_4$ + 3K$^+$, then another quadruplex (d(TGGGGT)$_4$) may stack at the 5’-end across a 5’-capping cation and form a dimeric structure (Fig. 5). Interestingly, the HOMO of this dimeric quadruplex structure (d(TGGGGT)$_8$+7K$^+$) is also localized on the 3’-guanine (Fig. 5). However, d(TGGGGT)$_8$+7K$^+$ (Fig. 5) has not been detected by ESI-MS, suggesting that this structure is unstable in water, and may be degraded by the applied high voltage and/or heated inert dry gas. However, the calculated HOMO localization is consistent with the experimental results for quadruplex DNA oxidations, suggesting that d(TGGGGT)$_8$+7K$^+$ is stably maintained in solution.

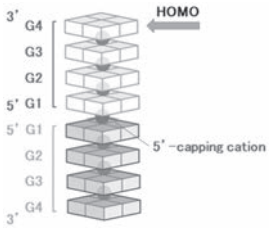

Fig. 5 The HOMO localization of the 5’-5’ stacked dimeric structure. The G-quartet plane and cations are shown as squares and circles.

Conclusion

HOMO localizations are closely associated with the site-specificities of guanine oxidation in various DNA structures. In double-stranded DNA, the 5’ side of GG steps is more easily oxidized than the 3’ side, and the HOMO is localized at the 5’ side of GG. Calculated HOMO energies are consistent with experimental vertical ionization potentials, and the HOMO is mainly localized on the base with the lowest ionization potential. N7 of the 3’-guanine is located just below the six-membered ring of the 5’-guanine in both B-form and A-form double-stranded DNA, and only this stacking geometry can result in HOMO localization. The calculated HOMO of quadruplex DNA indicates site-specificities of guanine oxidation, with 5’-guanines being mainly oxidized in d(TAGGGT)$_4$T and the HOMO being predominantly localized on the 5’-guanine. In contrast, 3’-guanine is mainly oxidized in d(TGGGGT)$_4$, and the HOMO is localized at the 3’-guanine in the quadruplex structure with a 5’-capping cation (d(TGGGGT)$_4$+4K$^+$) or in the dimeric quadruplex structure (d(TGGGGT)$_8$+7K$^+$). HOMO localization thus depends both on the DNA stacking geometry and the locations and number of metal ion cations.

This review discussed guanine oxidation in relation to computational approaches for HOMO localization. The reactivity of each local structure in cells can be predicted

from HOMO localization, allowing computational approaches to be applied to various intracellular DNA structures to explain the relationship between reactivity and DNA structure *in vivo*.

Acknowledgments

This work was supported from Tokushima Bunri University, and by research grants from LNest Grant L-RAD Award, from Radiation Effects Association, from the Nakatomi Foundation, from KAKENHI and from the Japan Prize Foundation. The author would like to thank Forte, Inc. (Tokyo) for the English language review.

References

1. Ito K, Kawanishi S. Photoinduced hydroxylation of deoxyguanosine in DNA by pterins: Sequence specificity and mechanism. Biochemistry, 1997; 36: 1774–1781.
2. Yanagawa H, Ogawa Y, Ueno M. Redox ribonucleosides. Isolation and characterization of 5-hydroxyuridine, 8-hydroxyguanosine, and 8-hydroxyadenosine from Torula yeast RNA. J Biol Chem, 1992; 267: 13320–13326.
3. Jovanovic SV, Simic MG. One-electron redox potentials of purines and pyrimidines. J Phys Chem, 1986; 90: 974–978.
4. Taylor JS, Cohrs MP. DNA, light, and Dewar pyrimidinones: the structure and biological significance of TpT_3. J Am Chem Soc, 1987; 109: 2834–2835.
5. Kino K, Sugiyama H. Possible cause of G·C→C·G transversion mutation by guanine oxidation product, imidazolone. Chem Biol, 2001; 8: 369–378.
6. Douki T, Reynaud-Angelin A, Cadet J, Sage E. Bipyrimidine photoproducts rather than oxidative lesions are the main type of DNA damage involved in the genotoxic effect of solar UVA radiation. Biochemistry, 2003; 42: 9221–9226.
7. Mouret S, Baudouin C, Charveron M, Favier A, Cadet J, Douki T. Cyclobutane pyrimidine dimers are predominant DNA lesions in whole human skin exposed to UVA radiation. Proc Natl Acad Sci USA, 2006; 103: 13765–13770.
8. Neeley WL, Essigmann JM. Mechanisms of formation, genotoxicity, and mutation of guanine oxidation products. Chem Res Toxicol, 2006; 19: 491–505.
9. Pratviel G, Meunier B. Guanine oxidation: One- and two-electron reactions. Chem Eur J, 2006; 12: 6018–6030.
10. Gimisis T, Cismaş C. Isolation, characterization, and independent synthesis of guanine oxidation products. Eur J Org Chem, 2006; 1351–1378.
11. Friedberg EC, Walker GC, Siede W, Wood RD, Schultz RA, Ellwnberger T. DNA Repair and Mutagenesis. Washington, DC: ASM Press, 2006.
12. Kino K, Kobayashi T, Arima E, Komori R, Kobayashi T, Miyazawa H. Photoirradiation products of flavin derivatives, and the effects of photooxidation on guanine. Bioorg Med Chem Lett, 2009; 19: 2070–2074.
13. Kino K, Morikawa M, Kobayashi T, Komori R, Sei Y, Miyazawa H. The oxidation of 8-oxo-7,8-dihydroguanine by iodine. Bioorg Med Chem Lett, 2010; 20: 3818–3820.
14. Kino K, Hirao-Suzuki M, Morikawa M, Sakaga A, Miyazawa H. Generation, repair and replication of guanine oxidation products. Genes Environ. 2017; 39: 1–8.
15. Kino K, Saito I, Sugiyama H. Product analysis of GG-specific photooxidation of DNA via electron transfer: 2-aminoimidazolone as a major guanine oxidation product. J Am Chem Soc, 1998; 120: 7373–7374.
16. Steenken S, Jovanovic SV. How easily oxidizable is DNA? One-electron reduction potentials of adenosine and guanosine radicals in aqueous solution. J Am Chem Soc, 1997; 119: 617–618.
17. Phillips K, Dauter Z, Murchie AIH, Lilley DMJ, Luisi B. The crystal structure of a parallel-stranded guanine tetraplex at 0.95Å resolution. J Mol Biol, 1997; 273: 171–182.
18. Haider S, Parkinson GN, Neidle S. Crystal structure of the potassium form of an Oxytricha nova G-quadruplex. J Mol Biol, 2002; 320: 189–200.
19. Parkinson GN, Lee MPH, Neidle S. Crystal structure of parallel quadruplexes from human telomeric DNA. Nature, 2002; 417: 876–880.
20. Simonsson T, Pecinka P, Kubista M. DNA tetraplex formation in the control region of c-myc. Nucleic Acids Res, 1998; 26: 1167–1172.
21. Phan AT, Modi YS, Patel DJ. Propeller-type parallel-stranded G-quadruplexes in the human c-myc promoter. J Am Chem Soc, 2004; 126: 8710–8716.
22. Aboul-ela F, Murchie AIH, Lilley DMJ. NMR study of parallel-stranded tetraplex formation by the hexadeoxynucleotide d(TG_4T). Nature, 1992; 360: 280–282.
23. Matsugo S, Kawanishi S, Yamamoto K, Sugiyama H, Matsuura T, Saito I. Bis(hydroperoxy)naphthaldiimide as a "photo-Fenton reagent": sequence-specific photocleavage of DNA. Angew Chem Int Ed, 1991; 30: 1351–1353.
24. Saito I. Photochemistry of highly organized biomolecules: Sequence-selective photoreaction of DNA. Pure Appl Chem, 1992; 64: 1305–1310.
25. Ito K, Inoue S, Yamamoto K, Kawanishis S. 8-Hydroxydeoxyguanosine formation at the 5' Site of 5'-GG-3' sequences in double-stranded DNA by UV radiation with riboflavin. J Biol Chem, 1993; 268: 13221–13227.
26. Saito I, Takayama M, Sugiyama H, Nakatani K, Tsuchida A, Yamamoto M. Photoinduced DNA cleavage via electron transfer: demonstration that

guanine residues located 5' to guanine are the most electron-donating sites. J Am Chem Soc, 1995; 117: 6406–6407
27. Saito I, Takayama M, Kawanishi S. Photoactivatable DNA-cleaving amino acids: highly sequence-selective DNA photocleavage by novel L-lysine derivatives. J Am Chem Soc, 1995; 117: 5590–5591.
28. Breslin DT, Schuster GB. Anthraquinone photonucleases: Mechanisms for GG-selective and nonselective cleavage of double-stranded DNA. J Am Chem Soc, 1996; 118: 2311–2319.
29. Williams TT, Dohno C, Stemp EDA, Barton JK. Effects of the photooxidant on DNA-mediated charge transport. J Am Chem Soc, 2004; 126: 8148–8158.
30. Saito I, Nakamura T, Nakatani K, Yoshioka Y, Yamaguchi K, Sugiyama H. Mapping of the hot spots for DNA damage by one-electron oxidation: Efficacy of GG doublets and GGG triplets as a trap in long-range hole migration. J Am Chem Soc, 1998; 120: 12686–12687.
31. Giese B, Amaudrut J, Köhler AK, Spormann M, Wessely S. Direct observation of hole transfer through DNA by hopping between adenine bases and by tunnelling. Nature, 2001; 412: 318–320.
32. Henderson PT, Jones D, Hampikian G, Kan Y, Schuster GB. Long-distance charge transport in duplex DNA: The phonon-assisted polaron-like hopping mechanism. Proc Natl Acad Sci USA, 1999; 96: 8353–8358.
33. Hall DB, Holmlin RE, Barton JK. Oxidative DNA damage through long-range electron transfer. Nature, 1996; 382: 731–735
34. Adhikary A, Khanduri D, Sevilla MD. Direct observation of the hole protonation state and hole localization site in DNA-oligomers. J Am Chem Soc, 2009; 131: 8614–8619.
35. Olmon ED, Hill MG, Barton JK. Using metal complex reduced states to monitor the oxidation of DNA. Inorg Chem, 2011; 50: 12034–12044.
36. Augustyn KE, Stemp EDA, Barton JK. Charge separation in a ruthenium-quencher conjugate bound to DNA. Inorg Chem, 2007; 46: 9337–9350.
37. Das P, Schuster GB. Effect of condensate formation on long-distance radical cation migration in DNA. Proc Natl Acad Sci USA, 2005; 102: 14227–14231.
38. Cao H. Schuster GB. Complex formation between a DNA duplex and lipid-like spermine derivatives: Hydrophobic protection of DNA from one-electron oxidation. Bioconj Chem, 2005; 16: 820–826.
39. Roberts LW. Schuster GB. Effect of netropsin on one-electron oxidation of duplex DNA. Photochem Photobiol, 2004; 80: 456.
40. Colson AO, Besler B, Close DM, Sevilla MD. Ab initio molecular orbital calculations of DNA bases and their radical ions in various protonation states: Evidence for proton transfer in GC base pair radical anions. J Phys Chem, 1992; 96: 661–668.
41. Sugiyama H, Saito I. Theoretical studies of GG-specific photocleavage of DNA via electron transfer: Significant lowering of ionization potential and 5'-localization of HOMO of stacked GG bases in B-form DNA. J Am Chem Soc, 1996; 118: 7063–7068.
42. Conwell EM. Charge transport in DNA in solution: The role of polarons. Proc Natl Acad Sci USA, 2005; 102: 8795–8799.
43. Blancafort L. Voityuk AA. CASSCF/CAS-PT2 study of hole transfer in stacked DNA nucleobases. J Phys Chem A, 2006; 110: 6426–6432.
44. Lewis FD, Letsinger RL, Wasielewski MR. Dynamics of photoinduced charge transfer and hole transport in synthetic DNA hairpins. Acc Chem Res, 2001; 34: 159–170.
45. Das P, Schuster GB. One-electron oxidation of condensed DNA toroids: Injection-site dependent charge (radical cation) mobility. Bioconj Chem, 2008; 19: 1235–1240.
46. Joy A, Ghosh AK, Schuster GB. One-electron oxidation of DNA oligomers that lack guanine: Reaction and strand cleavage at remote thymines by long-distance radical cation hopping. J Am Chem Soc, 2006; 128: 5346–5347.
47. Joy A, Guler G, Ahmed S, McLaughlin LW, Schuster GB. Polaronic semiconductor behavior of long-range charge transfer in DNA oligomers in solution: controlling barriers to long-distance radical cation migration in DNA with thymine analogs. Faraday Discuss, 2006; 131: 357–365.
48. Joy A, Schuster GB. Long-range radical cation migration in DNA: Investigation of the mechanism. Chem Commun, 2005; 2778–2784.
49. Giese B, Wessely S. The Influence of Mismatches on Long-Distance Charge Transport through DNA. Angew Chem Int Ed, 2000; 39: 3490–3491.
50. Giese B, Spichty M. Long Distance Charge Transport through DNA: Quantification and Extension of the Hopping Model. ChemPhysChem, 2000; 1: 195–198.
51. Saito I, Takayama M, Sugiyama H, Nakamura T. Design of photochemical DNA-cleaving molecules via electron transfer. Photochem Photobiol A, 1997; 106: 141–144.
52. Saito I, Nakamura T, Nakatani K. Mapping of highest occupied molecular orbitals of duplex DNA by cobalt-mediated guanine oxidation. J Am Chem Soc, 2000; 122: 3001–3006.
53. Morikawa M, Kino K, Oyoshi T, Suzuki M, Kobayashi T, Miyazawa H. Analysis of guanine oxidation products in double-stranded DNA and proposed guanine oxidation pathways in single-stranded, double-stranded or quadruplex DNA. Biomolecules, 2014; 4: 140–159.
54. Kumar A, Sevilla MD. Density functional theory studies of the extent of hole delocalization in one-

electron oxidized adenine and guanine base stacks. J Phys Chem B, 2011; 115: 4990–5000.
55. Giese B. Long-distance charge transport in DNA: The hopping mechanism. Acc Chem Res, 2000; 33: 631–636.
56. Schuster GB. Long-range charge transfer in DNA: Transient structural distortions control the distance dependence. Acc Chem Res, 2000; 33: 253–260.
57. Conwell EM, Basko DM. Hole traps in DNA. J Am Chem Soc, 2001; 123: 11441–11445.
58. Mantz YA, Gervasio FL, Laino T, Parrinello M. Charge localization in stacked radical cation DNA base pairs and the benzene dimer studied by self-interaction corrected density-functional theory. J Phys Chem A, 2007; 111: 105–112.
59. Bixon M, Jortner J. Long-range and very long-range charge transport in DNA. Chem Phys, 2002; 281: 393–408.
60. Prat F, Houk KN, Foote CS. Effect of guanine stacking on the oxidation of 8-oxoguanine in B-DNA. J Am Chem Soc, 1998; 120: 845–846.
61. Patel DJ, Phan AT, Kuryavyi V. Human telomere, oncogenic promoter and 5′-UTR G-quadruplexes: Diverse higher order DNA and RNA targets for cancer therapeutics. Nucleic Acids Res, 2007; 35: 7429–7455.
62. Morikawa M, Kino K, Oyoshi T, Suzuki M, Kobayashi T, Miyazawa H. Calculation of the HOMO localization of Tetrahymena and Oxytricha telomeric quadruplex DNA. Bioorg Med Chem Lett, 2015; 25: 3359–3362.
63. Fleming AM, Zhu J, Howpay Manage SA, Burrows CJ. Human NEIL3 gene expression regulated by epigenetic-like oxidative DNA modification. J Am Chem Soc, 2019; 141: 11036–11049.
64. Morikawa M, Kino K, Oyoshi T, Suzuki M, Kobayashi T, Miyazawa H. Product analysis of photooxidation in isolated quadruplex DNA; 8-oxo-7,8-dihydroguanine and its oxidation product at 3′-G are formed instead of 2,5-diamino-4H-imidazol-4-one. RSC Adv, 2013; 3: 25694–25697.

Estimating the local temperature of human serum albumin photoirradiated in the presence of a fluorescent dye by measuring the intrinsic fluorescence

Kazutaka Hirakawa[1,2,*] and Minori Uemura[1]

[1] *Department of Applied Chemistry and Biochemical Engineering, Faculty of Engineering, Shizuoka University, Johoku 3-5-1, Naka-ku, Hamamatsu, Shizuoka 432-8561, Japan*
[2] *Department of Optoelectronics and Nanostructure Science, Graduate School of Science and Technology, Shizuoka University, Johoku 3-5-1, Naka-ku, Hamamatsu, Shizuoka 432-8561, Japan*

***Corresponding author:**
Kazutaka Hirakawa
Department of Applied Chemistry and Biochemical Engineering, Faculty of Engineering, Shizuoka University, Johoku 3-5-1, Naka-ku, Hamamatsu, Shizuoka 432-8561, Japan
Tel/Fax: +81-53-478-1287, E-mail: hirakawa.kazutaka@shizuoka.ac.jp

ABSTRACT

The photothermal conversion effect of a fluorescent dye binding on protein was evaluated by measuring the fluorescence intensity of amino acid residue. The intrinsic fluorescence intensity of tryptophan residue in human serum albumin, a water-soluble protein, decreased with an increase in the temperature. This phenomenon could be explained by the enhancement of the nonradiative transition of the photoexcited state of tryptophan, and the activation energy of this process could be roughly estimated. The relationship between the fluorescence intensity and temperature was used as the calibration curve to estimate the local temperature of human serum albumin. Rhodamin-110, a fluorescent dye, and human serum albumin were mixed and photoirradiated with a light-emitting diode. The fluorescence intensity of the tryptophan residue was decreased by photoirradiation with the dye, and the local temperature of human serum albumin could be estimated. The estimated rate of temperature rise was 1.0 K min^{-1} in the case of 5 μM rhodamine-110 and 10 μM human serum albumin with visible light irradiation (468 nm, 4.0 mW cm^{-2}). The inactivation of tyrosinase by rhodamine-110 with visible light irradiation was also evaluated.

Keywords: Photothermal effect; Human serum albumin; Tryptophan; Fluorescence; Rhodamine-110

INTRODUCTION

Photothermal conversion is an important application of photophysical processes for medical uses such as photothermal therapy [1,2]. The temperature in a biological environment is important data for evaluating photothermal conversion and photothermal therapy. Various nanomaterials have been studied for evaluating the cellular temperature [3]. For example, cationic fluorescent polymers can indicate the temperature in vivo by the changing fluorescence intensity [4-6]. Although the temperature of small materials, *i.e.*, the molecular temperature, is a difficult concept [7], the local temperature of biomacromolecules such as proteins may be used to evaluate the activity of the light absorber for photothermal conversion. The purpose of this study is to apply the intrinsic fluorescence of protein to estimate the local temperature. In general, the fluorescence intensity of molecules depends on the temperature, and the intrinsic fluorescence of amino acid residue in protein depends on the local microenvironment [8]. In this study, human serum albumin (HSA) was used as a model protein. The X-ray structure and amino acid sequence of HSA have been clarified, and HSA has one tryptophan residue [9], which can emit relatively strong fluorescence [10]. Since tryptophan residue of HSA, the fluorophore, is one, it is expected that the local temperature can be simply evaluated. The fluorescence of tryptophan depends on the environment of surroundings [11-13]. It was reported that tryptophan fluorescence is varied by the quenching through electron transfer from the indole ring to the amide group or to the hydrogen bonds of the surrounding water [14]. The fluorescence lifetime of tryptophan R-form rotamer is longer than that of B-form rotamer and their values depend on the temperature [15]. Therefore, the fluorescence intensity of tryptophan of HSA is considered to be varied by the microenvironmental condition depending on the temperature. Fluorescent dye is considered to be useful as a light absorber, because fluorescent dyes barely induce oxidative damage to biomacromolecules. Thus, rhodamine-110 (RH-110, Fig. 1), a fluorescent

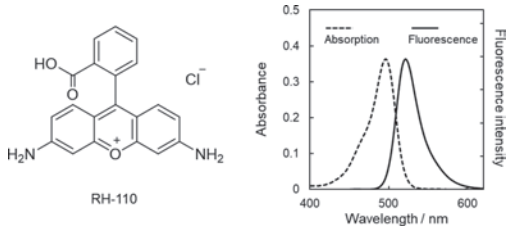

Fig. 1 The structure of RH-110 (left), and its absorption and fluorescence spectra (right). The presented fluorescence intensity is an arbitrary unit.

molecule, was used as the light absorber. RH-110 cannot induce DNA damage [16], and its photosensitized singlet oxygen production activity is also negligibly small [17]. In addition, a gold nanoparticle, which absorbs light through the surface plasmon resonance, resulting in the photothermal conversion [18], was also used as a light absorber.

EXPERIMENTAL

RH110 and HSA were purchased from Sigma-Aldrich Co. LLC. (St. Louis, MO, USA). Sodium phosphate buffer (0.1 M, pH 7.6) was from Nacalai Tesque, Inc. (Kyoto, Japan). Polyvinylpyrrolidone K 30 (PVP) was from Tokyo Chemical Industry Co., Ltd. (Tokyo Japan). Tryptophan and tyrosine were from FUJIFILM Wako Pure Chemical Co., Ltd. (Osaka, Japan). These chemical agents were used as received. PVP-protected gold nanoparticles (Au-PVP, average diameter: 10 nm) were prepared by previous report [19]. The sample solution containing HSA and RH-110 or Au-PVP in a 10 mM sodium phosphate buffer (pH 7.6) was irradiated with a light emitting diode (LED, 4.0 mW cm^{-2}, CCS Inc., Kyoto, Japan). A blue LED (λ_{max}= 468 nm) and a green LED (λ_{max}= 519 nm) were used for RH-110 and Au-PVP, respectively. The absorption spectra of samples were measured with the UV-VIS spectrophotometer UV-1650PC (Shimadzu, Kyoto, Japan). The fluorescence spectra of samples were measured with an F-4500 fluorescence spectrophotometer (Hitachi, Tokyo, Japan). The fluorescence intensity of HSA at 350 nm was measured with a fluorescence photometer 650-60 (Hitachi). The fluorescence lifetime (τ_f), which equals the singlet excited-state (S_1) lifetime, of HSA was measured with a Fluorescence Lifetime System TemPro (HORIBA, Kyoto, Japan). The excitation wavelength for the fluorescence measurements was 294 nm. To evaluate the enzyme activity, a sample solution containing tyrosinase (Sigma-Aldrich Co. LLC.) and RH-110 was irradiated with the blue LED for 2 hours, as previously reported [20]. After irradiation, tyrosine was added, and the samples were held at 37 ℃ for 1 hour. The enzymatic activity of tyrosinase was evaluated by measuring the absorption spectrum of oxidized tyrosine.

RESULTS AND DISCUSSION

The absorption spectrum of tryptophan (Fig. 2A) in a 10 mM sodium phosphate buffer (pH 7.6) was independent of the temperature, whereas the fluorescence intensity of tryptophan decreased with an increase in temperature (Fig. 2B). Relevantly, it was reported that τ_f of tryptophan decreased with an increase in temperature in the range of 9.1 ~ 74.6 ºC [11]. In general, the fluorescence quantum yield (Φ) is expressed using the rate constants of radiative transition (k_r) and nonradiative transition (k_{nr}) [21]; and the k_{nr} can be estimated using the following equation:

$$k_{nr} = \left(\frac{1}{\Phi} - 1\right) k_r \qquad (1).$$

The k_r is the same as the rate constant of the fluorescence process (k_f). It was reported that the k_f of tryptophan is temperature independent [11]. The k_f could be calculated by the following equation:

$$k_r = k_f = \frac{\Phi_0}{\tau_0} \qquad (2),$$

where Φ_0 (0.14) [22] and τ_0 are the fluorescence quantum yield under the standard condition (298 K) and that of τ_f, respectively. The average τ_f value (τ_f^{Av}) was calculated from the observed τ_f of tryptophan (2.79 ns (τ_1), 90% (a_1); 7.21 ns (τ_2), 10% (a_2)) using the following equation:

$$\tau_f^{Av} = \sum a_i \tau_i \ (i = 1, 2\ldots) \qquad (3).$$

The obtained value (3.23 ns) was used for the τ_0 in the equation (2). The Arrhenius plot using the k_{nr} and the

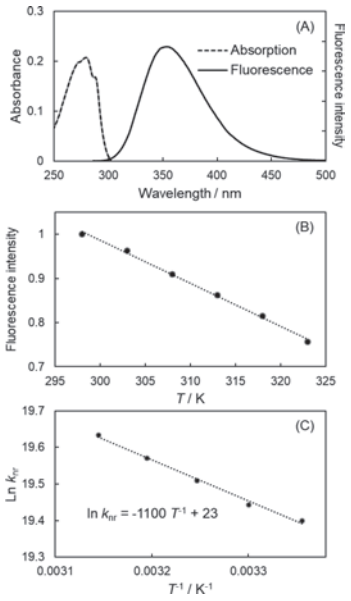

Fig. 2 The absorption and fluorescence spectra of tryptophan (A). The sample solution contained 100 μM (absorption) or 50 μM tryptophan in a 10 mM sodium phosphate buffer (pH 7.6). The excitation wavelength for fluorescence measurement was 279 nm. The fluorescence intensity of 50 μM tryptophan under the indicated temperature (B). The Arrhenius plot of the k_{nr} (C). The Arrhenius equation, Ln k_{nr} = -E_a/RT + Ln A, where R is the gas constant and A is the preexponential factor, was used. The presented fluorescence intensity is an arbitrary unit.

absolute temperature of the solution (T) demonstrated that the activation energy of the nonradiative transition (E_a) is 9.3 kJ mol^{-1} (Fig. 2C). The observed value was comparable to that of cyanine dyes (8.8 and 14.2 kJ mol^{-1}) in an aqueous solution [23], and was smaller than that of other organic molecules in nonpolar solvents (around 20~30 kJ mol^{-1}) [24]. The reported E_a value for the nonradiative transition in the triplet excited state (T_1) of tryptophan under low temperature (44.2 kJ mol^{-1}, 170~200 K, in a 3:1 (v/v) glycerol/water mixture) [25] is larger than the presented E_a value in the S_1 of tryptophan.

Similar to the case of tryptophan, the absorption spectrum of HSA (Fig. 3A) was barely affected by temperature, whereas the fluorescence intensity of tryptophan residue was decreased reversibly with an increase in temperature (Fig. 3B). These results could be explained by the fact that the relaxation process of the photoexcited tryptophan residue of HSA is enhanced by the temperature rise. It was reported that the degree of HSA folding was found to be kept from 1.0 at 298 K to ~0.7 at 353 K [26]. In this study, the linear relationship between the fluorescence intensity and temperature was observed in the range of 283 ~ 353 K. Furthermore, the activation energy of HSA unfolding increases significantly in the presence of binding molecule [27]. Therefore, it is considered that the effect of HSA denaturation is negligibly small in this experimental condition. This linear relationship between the fluorescence intensity at 350 nm and the temperature was used as the calibration curve to estimate the local temperature of protein. Similar to the case of tryptophan solution, the k_{nr} of HSA was estimated using the Φ_0 (0.11) [28] and τ_0 of tryptophan residue in HSA. The τ_0 of HSA (5.61 ns) was calculated from the observed τ_f of tryptophan residue in HSA (7.99 ns (τ_1), 48% (a_1); 3.81 ns (τ_2), 45% (a_2); 0.93 ns (τ_3), 7% (a_3)) using the equation (3). The E_a value of HSA estimated from the Arrhenius plot (Fig. 3C, 5.6 kJ mol^{-1}) was smaller than that of the above-mentioned free tryptophan. These findings suggest that the nonradiative transition of tryptophan in a condensed phase such as protein is more sensitive than that of the solution condition. The observed E_a value is smaller than that of the nonradiative transition in the T_1 of HSA (22.4 kJ mol^{-1}, 170~200 K, in 3:1 (v/v) glycerol/water mixture) [25].

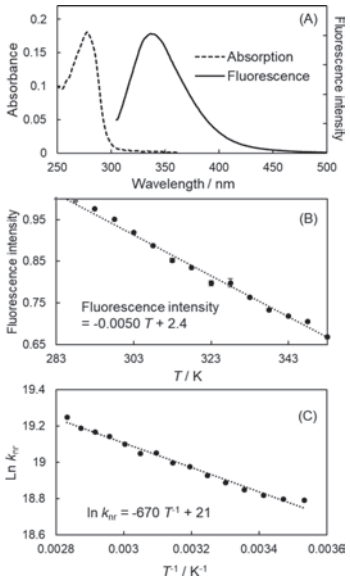

Fig. 3 The absorption and fluorescence spectra of HSA (A). The sample solution contained 10 μM HSA in a 10 mM sodium phosphate buffer (pH 7.6). The excitation wavelength for fluorescence measurement was 298 nm. The fluorescence intensity of HSA under the indicated temperature (B). The Arrhenius plot for the k_{nr} (C). The Arrhenius equation is presented in the legend of Fig. 2. The presented fluorescence intensity is an arbitrary unit.

RH-110 absorbs visible light (450~500 nm) and emits strong fluorescence at around 520 nm (Fig. 1). HSA cannot be photoexcited by visible light. Photoirradiation with the blue LED did not affect the fluorescence intensity of HSA. The fluorescence intensity of tryptophan residue in HSA was gradually decreased by photoirradiation with RH-110 (Fig. 4A). Because RH-110 does not induce the photooxidation of biomolecules [16], the observed results can be explained by the thermal effect. The absorption spectrum of RH-110 at around 500 nm, which is not absorbed by HSA, was slightly increased and shifted by the addition of HSA, suggesting a static association between RH-110 and HSA (data not shown). Relevantly, it has been reported that phenothiazine dyes, similar size cationic dyes as RH-110, bind to HSA through hydrophobic interaction and the absorption spectral change of dyes through the interaction with HSA is small [29]. It is speculated that hydrophobic interaction between RH-110 and HSA is the main binding force. The τ_f of HSA was slightly decreased by RH-110. The extent of decreased τ_f by RH-110 is comparable to the case of a cationic porphyrin, which binds on the surface of HSA [30]. Analysis by the Förster resonance energy transfer (FRET) method [31] showed that the average distance between RH-110 and the tryptophan residue of HSA is 38–48 Å. Since the average diameter of HSA is about 80 Å [32], these experimental results suggest that RH-110 molecules bind to the HSA surface. These findings suggest that photoirradiated RH-110 binding to the HSA surface converts the photoenergy to heat, leading to the decrease of the fluorescence intensity of HSA. Using the above-mentioned calibration curve (Fig. 3B), the temperature rise (ΔT) was calculated (Fig. 4C). The rate of the ΔT ($R_{\Delta T}$) was estimated from the initial time profile of the ΔT (Fig. 4C), and the obtained value was 1.0 K min^{-1} in this experimental condition.

The thermal inactivation of tyrosinase by RH-110 with visible light irradiation was evaluated. Tyrosinase catalyzes the oxidation of tyrosine to DOPA-quinone [33]. This enzyme activity can be examined by UV-VIS absorption measurement of the formed quinones, as previously reported [20]. The typical absorption spectrum was observed after the incubation of tyrosine in the presence of tyrosinase at around 500 nm. The tyrosine

oxidation activity of tyrosinase was completely inactivated (less than the noise level) by photoirradiation with RH-110 in this experimental condition (Table 1). RH-110 itself without photoirradiation did not inactivate the tyrosinase activity. The tyrosinase activity irradiated without RH-110 decreased to 50% of the untreated tyrosinase. These results suggest that the photoirradiation itself induces the inactivation of tyrosinase in this experimental condition, and the irradiated RH-110 can greatly inactivate tyrosinase via photothermal conversion.

The photothermal effect of a gold nanoparticle was also evaluated qualitatively using the intrinsic fluorescence of HSA. PVP, a neutral water-soluble polymer, was used as a protective colloid of gold nanoparticle. Because PVP can stabilize the metal nanoparticles including gold nanoparticle [34,35], PVP is expected to prevent an aggregation of gold nanoparticle through an interaction with protein. Photoirradiation with Au-PVP decreased the fluorescence intensity of the tryptophan residue of HSA (Fig. 4B). In general, a metal nanoparticle is larger than organic dyes, and its size is comparable to that of protein [19,36]. Therefore, the evaluation of the binding interaction between a metal nanoparticle and protein is difficult. The estimated $R_{\Delta T}$ was 0.14 K min^{-1} in this experimental condition (Fig. 4C). These obtained values were corrected by the mass of light absorbers (RH-110 and Au-PVP) and the number of photons absorbed by these light absorbers, which was estimated from the overlap between the absorption spectrum of the light absorber and the emission spectrum of the LED (Table 2). Because the association ratio of these light absorbers is unclear, the listed values are qualitative characteristics of these materials for photothermal conversion. The relatively small value for the $R_{\Delta T}$ per mass in the case of Au-PVP is due to that gold

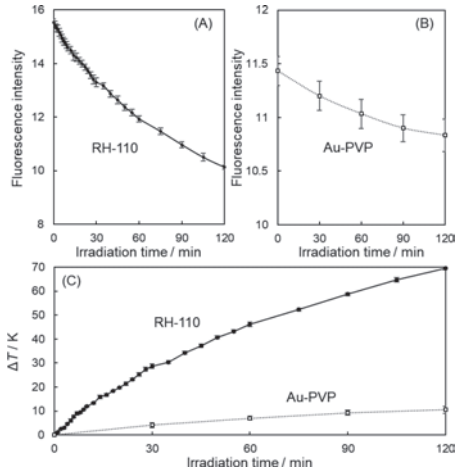

Fig. 4 Fluorescence intensity of HSA photoirradiated with RH-110 (A) or Au-PVP (B). The sample solution contained 10 μM HSA and 5 μM RH-110 or 50 μM (atomic concentration of gold) Au-PVP in a 10 mM sodium phosphate buffer (pH 7.6) was irradiated with an LED (λ_{max} = 468 nm (RH-110) or 519 nm (Au-PVP), 4.0 mWcm^{-2}). The ΔT was calculated using the calibration curve (Fig. 3B).

Table 1 Thermal inactivation of tyrosinase by RH-110 with visible light irradiation

Condition	Photoirradiation	RH-110	Catalytic reaction rate / μmol min^{-1}
Control 1	-	-	1.00
Control 2	-	+	1.09
Control 3	+	-	0.50
Test sample	+	+	~ 0

The sample solution containing 5 μM RH-110 and 10 units of tyrosinase in a 10 mM sodium phosphate buffer (pH 7.6) was irradiated with a blue LED (λ_{max} = 468 nm, 4.0 mWcm^{-2}, 2 hours). One unit of tyrosinase can oxidize 1.7 nmol tyrosine per min.

Table 2 The rate and efficiency of photothermal conversion by RH-110 and Au-PVP

Light absorbaer	RH-110	Au-PVP
$R_{\Delta T}$ / K min^{-1}	1.0	0.14
$R_{\Delta T}$ per mass / K min^{-1} mg^{-1}	460	12
ΔT per absorbed photons / K μmol^{-1}	2.9	18
E_{PTC} / K nJ^{-1} *	11	72

The sample solution containing 5 μM HSA and 5 μM RH-110 or 50 μM (atomic concentration of gold) Au-PVP in a 10 mM sodium phosphate buffer (pH 7.6) was irradiated with an LED (λ_{max} = 468 nm or 519 nm, 4.0 mWcm^{-2}). *: E_{PTC} = (ΔT per absorbed photons) ÷ ($h\ c\ N_A/\lambda$), where h is the Plank constant, c is light velocity, N_A is the Avogadro constant, and λ is the wavelenght of irradiated light (468 nm or 519 nm).

nanoparticle is a relatively heavy material. The absorption photons per mass of high density material becomes smaller than that of the low density material. The larger values for ΔT per absorbed photons and the efficiency of photothermal conversion (E_{PTC}, Table 2) in the case of Au-PVP suggest that the photothermal conversion effect by the surface plasmon resonance of gold is relatively large, whereas most photoexcitation energy of RH-110 is used for fluorescence emission.

CONCLUSIONS

The intrinsic fluorescence intensity of the tryptophan residue of HSA decreased with an increase in temperature. This phenomenon could be used to estimate the local temperature of the visible light-irradiated HSA with a light absorber. In the presence of RH-110, the temperature can be estimated to rise by about 10 K in the following condition (468 nm, 4.0 mW cm^{-1}, 10 min). The inactivation of tyrosinase by visible light irradiation with RH-110 was also evaluated. These results suggest that the intrinsic fluorescence intensity can be used to probe the local temperature of biological materials.

Acknowledgments

This work was supported in part by Grant-in-Aid for Scientific Research (B) from Japanese Society for the Promotion of Science (JSPS KAKENHI 17H03086).

Notes

The authors declare no conflict of interests.

References

[1] Liu Y, Bhattarai P, Dai Z, Chen X. Photothermal therapy and photoacoustic imaging via nanotheranostics in fighting cancer. Chem. Soc. Rev., 2019;48:2053–2108.

[2] Hu K, Xie L, Zhang Y, Hanyu M, Yang Z, Nagatsu K, Suzuki H, Ouyang J, Ji X, Wei J, Xu H, Farokhzad OC, Liang SH, Wang L, Tao W, Zhang MR. Marriage of black phosphorus and Cu^{2+} as effective photothermal agents for PET-guided combination cancer therapy. Nat. Commun., 2020;11:2778.

[3] Nakano M, Nagai T. Thermometers for monitoring cellular temperature. J. Photochem. Photobiol. C: Photochemistry Rev., 2017;30:2–9.

[4] Tsuji T, Yoshida S, Yoshida A, Uchiyama S. Cationic fluorescent polymeric thermometers with the ability to enter yeast and mammalian cells for practical intracellular temperature measurements. Anal. Chem., 2013;85:9815–9823.

[5] Uchiyama S, Tsuji T, Ikado K, Yoshida A, Kawamoto K, Hayashi T, Inada N. A cationic fluorescent polymeric thermometer for the ratiometric sensing of intracellular temperature. Analyst, 2015;140:4498–4506.

[6] Okabe K, Sakaguchi R, Shi B, Kiyonaka S. Intracellular thermometry with fluorescent sensors for thermal biology. Eur. J. Phys., 2018;470:717–731.

[7] Phares DJ, Srinivasa AR. Molecular dynamics with molecular temperature. J. Phys. Chem. A, 2004;108:6100–6108.

[8] McCaslin TG, Pagba CV, Chi SH, Hwang HJ, Gumbart JC, Perry JW, Olivieri C, Porcelli F, Veglia G, Guo Z, McDaniel M, Barry BA. Structure and function of tryptophan-tyrosine dyads in biomimetic beta hairpins. J. Phys. Chem. B, 2019;123:2780–2791.

[9] He XM, Carter DC. Atomic structure and chemistry of human serum albumin. Nature, 1992;358:209–215.

[10] Hirakawa K, Suzuki A, Ouyang D, Okazaki S, Ibuki Y, Nakazaki J, Segawa H. Controlled photodynamic action of axial fluorinated diethoxyP(V)tetrakis(*p*-methoxyphenyl)porphyrin through self-aggregation. Chem. Res. Toxicol., 2019;32:1638–1645.

[11] Robbins RJ, Fleming GR, Beddard GS, Robinson GW, Thistlethwaite PJ, Woolfe GJ. Photophysics of aqueous tryptophan: pH and temperature effects. J. Am. Chem. Soc., 1980;102:6271–6279.

[12] Dashnau JL, Zelent B, Vanderkooi JM. Tryptophan interactions with glycerol/water and trehalose/sucrose cryosolvents: infrared and fluorescence spectroscopy and ab initio calculations. Biophys. Chem., 2005;114:71–83.

[13] Schlamadinger DE, Gable JE, Kim JE. Hydrogen bonding and solvent polarity markers in the UV resonance Raman spectrum of tryptophan: application to membrane proteins. J. Phys. Chem. B, 2009;113:14769–14778.

[14] Knox PP, Gorokhov VV, Korvatovsky BN, Grishanova NP, Goryachev SN, Paschenko VZ. Specific features of the temperature dependence of tryptophan fluorescence lifetime in the temperature range of −170–20 °C. J. Photochem. Photobiol. A: Chem., 2020;393:112435.

[15] Gorokhov VV, Knox PP, Korvatovskiy BN, Seifullina NK, Goryachev SN, Paschenko VZ. Temperature dependence of tryptophan fluorescence lifetime in aqueous glycerol and trehalose solutions. Biochemistry (Mosc), 2017;82:1269–1275.

[16] Hirakawa K, Ochiai S, Oikawa S, Kawanishi S. Oxygen-independent DNA damage photosensitized by rhodamine-6G. Trends Photochem. Photobiol., 2011;13:29–35.

[17] Hirakawa K, Ito H. Rhodamine-6G can photosensitize folic acid decomposition through electron transfer. Chem. Phys. Lett., 2015;627:26–29.

[18] Kim M, Lee JH, Nam JM. Plasmonic photothermal nanoparticles for biomedical applications. Adv. Sci., 2019;6:1900471.

[19] Hirakawa K, Sano S. Platinum nanoparticle catalyst scavenges hydrogen peroxide generated from hydroquinone. Bull. Chem. Soc. Jpn., 2009;82:1299–

1303.
[20] Ouyang D, Hirakawa K. Photosensitized enzyme deactivation and protein oxidation by axial-substituted phosphorus(V) tetraphenylporphyrins. J. Photochem. Photobiol. B: Biol., 2017;175:125–131.
[21] Inai N, Yokogawa D, Yanai T. Investigating the nonradiative decay pathway in the excited state of silepin derivatives: a study with second-order multireference perturbation wavefunction theory. J. Phys. Chem. A, 2021;125:559−569.
[22] Chen RF, Fluorescence quantum yields of tryptophan and tyrosine. Anal. Lett., 1967;1:35–42.
[23] Yarmoluk SM, Losytskyy MY, Yashchuk VM. Nonradiative deactivation of the electronic excitation energy in cyanine dyes: influence of binding to DNA. J. Photochem. Photobiol. B: Biol., 2002;67:57–63.
[24] Patil NR, Melavanki RM, Thipperudrappa J, Afi UO. Effect of temperature on the fluorescence emission of ENCTTTC in different nonpolar solvents. Can. J. Phys., 2013;91:971–975.
[25] Draganski AR, Friedman JM, Ludescher RD. Solvent-slaved dynamic processes observed by tryptophan phosphorescence of human serum albumin. Biophys. J., 2017;112:881–891.
[26] Mohan V, Sengupta B, Acharyya A, Yadav R, Das N, Sen P. Region-specific double denaturation of human serum albumin: combined effects of temperature and GnHCl on structural and dynamical responses. ACS Omega, 2018;3:10406–10417.
[27] Preisz Z, Kunsági-Máté S. Effect of methotrexate and its photodegradation products on the temperature induced denaturation of human serum albumin. Spectrochim. Acta A: Mol. Biomol. Spectrosc., 2021;245:18905.
[28] Sytnik A, Litvinyuk I. Energy transfer to a proton-transfer fluorescence probe: Tryptophan to a flavonol in human serum albumin. Proc. Natl. Acad. Sci. USA, 1996;93:12959–12963.
[29] Hirakawa K, Ishikawa T. Phenothiazine dyes photosensitize protein damage through electron transfer and singlet oxygen generation. Dyes Pigm., 2017;142:183−188.
[30] Hirakawa K, Takai S, Horiuchi H, Okazaki S. Photooxidation activity control of dimethylaminoph enyltris-(*N*-methyl-4-pridinio)porphyrin by pH. ACS Omega, 2020;5:27702−27708.
[31] Förster, T. Zwischenmolekulare energiewanderung und fluoreszenz. Ann. Phys., 1948:437:55−75.
[32] Ferrer ML, Duchowicz R, Carrasco B, de la Torre JG, Acuña AU. The conformation of serum albumin in solution: a combined phosphorescence depolarization-hydrodynamic modeling study. Biophys. J., 2001;80:2422–2430.
[33] Ramsden CA, Riley PA. Tyrosinase: the four oxidation states of the active site and their relevance to enzymatic activation, oxidation and inactivation. Bioorg. Med. Chem., 2014;22:2388–2395.
[34] Toshima N, Kushihashi K, Yonezawa T, Hirai H. Colloidal dispersions of palladium-platinum bimetallic clusters protected by polymers. Preparation and application to catalysis. Chem. Lett., 1989;1769–1772.
[35] Chili MM, Pullabhotla VSRR, Revaprasadu N. Synthesis of PVP capped gold nanoparticles by the UV-irradiation technique. Mater. Lett., 2011;65: 2844−2847.
[36] Hirakawa K, Kaneko T, Toshima N. Kinetics of spontaneous bimetallization between silver and noble metal nanoparticles. Chem. Asian J., 2018;13:1892–1896.

A novel method for locating nucleosomes by exploiting 5-bromouracil, pyrene-modified histone, and photoirradiation

Fumitaka Hashiya[1], and Hiroshi Sugiyama[1,2]

[1] *Department of Chemistry, Graduate School of Science, Kyoto University, Kitashirakawa-Oiwakecho, Sakyo-ku, Kyoto 606-8502, Japan*
[2] *Institute for Integrated Cell-Material Sciences (WPI-iCeMS), Kyoto University, Yoshida-Ushinomiyacho, Sakyo-ku, Kyoto 606-8501, Japan*

Keywords: nucleosome, 5-bromouracil, pyrene, photoreaction

ABSTRACT

Locating nucleosomes is an essential technique in molecular biology and great efforts have been made to improve the technique. Conventional methods are effective for the analysis of chromatin structures on genome DNA; however, they are not capable of evaluating the dynamic translocation of the nucleosome in chromatin dynamics because of their limited time scale and resolution. In the present work, a rapid and high-resolution method for locating nucleosomes was developed that exploits photoirradiation of pyrene-modified histone and bromouracil-substituted DNA. Using the method, 20 seconds of photoirradiation was sufficient to generate DNA cleavage on both the entry and exit sites of the nucleosome. The approach was thus used to analyze the interaction between DNA and the histone tail domain. The results show that the C terminal of histone H2A variant interacts with DNA at the entry or exit sites of the nucleosome, although the C terminal was located on the dyad part of the nucleosome in a molecular dynamics simulation.

INTRODUCTION

A nucleosome comprised of two H2A–H2B and H3–H4 histone heterodimers covering 146 bp DNA is the minimum unit of the chromatin structure.[1] The chromatin structure contributes to regulating gene expression and DNA repair by either restricting or facilitating protein access to genome DNA. Recent studies have revealed that nucleosomes are translocated by chromatin remodeling proteins to alter chromatin structure, and the dynamic change of chromatin is essential for maintaining genome functions. The translocation is mainly monitored by FRET, in which both DNA and histone are labeled with fluorescence dye, and several insights including translocation speed have been obtained.[2] However, the method is only suitable for single nucleosomes and it is difficult to monitor genome-wide changes. MNase-Seq is an analytical approach in which chromatin is digested with micrococcus nuclease to obtain DNA fragments covered with nucleosome that are then analyzed using high-throughput sequencing. Although it is an effective method to locate nucleosomes, it requires tens of minutes to digest chromatin. Considering that translocating processes are generally completed within one minute,[2] MNase-Seq is not practical to monitor the dynamic changes in chromatin, and a new method that can be used to locate nucleosomes within this short timeframe with high resolution is required.

5-Bromouracil (^{Br}U) is a photoreactive analogue of thymine that does not significantly interfere with DNA–protein interactions; thus, thymine can be replaced with ^{Br}U in conventional DNA replication systems, including PCR. UV irradiation facilitates electron transfer from aromatic moieties including aromatic amino acid residues and nucleotide bases to ^{Br}U and generates a reactive uracil radical, resulting in strand cleavage. The electron donor must be positioned within several angstroms of the ^{Br}U for electron transfer to occur; thus, ^{Br}U is an attractive probe with which to evaluate the interaction between DNA and DNA-binding molecules.[3] Previously, we demonstrated that modification of pyrene as an electron donor enhanced the photosensitivity of the electron transfer and this phenomenon was used to locate DNA-binding molecules after short photoirradiation.[4] In the present work, we introduced a pyrene modification on the tail domain of histone and demonstrate the electron transfer from the modified histone to ^{Br}U-substituted DNA in the nucleosome. Electron transfer was facilitated by photoirradiation and led to DNA cleavage on either the entry or exit sites of the nucleosome, although the modification was deposited close to the nucleosome dyad in molecular dynamics (MD) simulation.[5] These results suggest that the photoirradiation of nucleosome comprised of pyrene-modified histone and ^{Br}U-substituted DNA is an attractive technique that can be used not only to locate nucleosomes but also evaluate histone tail and DNA interactions.

MATERIALS AND METHODS

Preparation of H2A Mutants and Pyrene Modification

H124C or A126C histone H2A mutant expression plasmids were prepared with KOD-Plus-Mutagenesis

Kit (TOYOBO) from wild-type histone H2A expression plasmid by following the manufacturer's protocol. *Escherichia coli* strain BL21(DE3) was transformed with the expression plasmid and disrupted by freeze and thaw. H2A variants were purified from the lysate using HiTrap SP ion exchange column (GE Healthcare). H3 and H4 variants were also prepared using the same strategy.

H2A mutant (1 mM) and *N*-(1-pyrenyl) maleimide (10 mM) were dissolved in reaction buffer (20 mM Tris-HCL (pH 7.5), 2 M guanidine chloride, 25% ethanol, and 25% acetone) and pyrene modification was performed at room temperature for 3 hours in the dark. The reaction mixture was freeze-dried and dissolved in water to precipitate *N*-(1-pyrenyl) maleimide. Subsequently, the supernatant was purified by HPLC with C18 reverse-phase column (NACALAI) to obtain pyrene-modified A126A. The molecular weight of the histone variants was measured with a MALDI-TOF MS, Microflex Reflectron-KS II system (BRUKER) with sinapic acid used as the matrix.

Nucleosome Reconstitution

Unfolded H2A and H2B (each 250 μM) were dialyzed against refolding buffer (20 mM HEPES–KOH (pH 7.5), 2 M NaCl, and 5 mM DTT) for 12 hours at 4 °C to reconstitute the H2A–H2B heterodimer. The dialyzed sample was then purified with a Superdex 200 size-exclusion column (GE Healthcare). The H3–H4 heterotetramer was also prepared by the same scheme.

A DNA fragment that contained a 146 bp 601 sequence flanked with 130 bp extra sequences was prepared by PCR using Taq DNA polymerase. In the PCR, dBrUTP was used instead of dTTP and one of the primers was labeled with Texas Red for following slab gel sequencing.

DNA (200 nM), H2A–H2B heterodimer (200 nM), and H3–H4 heterotetramer (200 nM) were mixed in refolding buffer and dialyzed against reconstitution buffer (20 mM HEPES–KOH (pH 7.5), and 1 mM DTT) for 12 hours at 4 °C. The reconstitution was confirmed by PAGE analysis in which 200 V constant voltage electrophoresis was performed for 60 min with 6% of native acryl amide gel. The reconstituted nucleosome and free DNA was observed by LAS-3000UVmini (FUJIFILM) with ethidium bromide staining.

Locating Nucleosome by Photoirradiation

The reconstituted nucleosome prepared above was irradiated with 365 nm UV for 0, 20, 40, or 60 sec on ice using ZUV-C30H (OMRON) with ZUV-H30M head unit. The irradicated sample subsequently treated with uracil DNA glycosylase (NEB) at 37 °C for 1 hour to remove uracil base. The sample was dissolved in gel loading buffer (15 mM EDTA·2Na and 99.5% formamide) and incubated at 90 °C for 5 min to cleave DNA at abasic sites. The cleavage sites were located with an SQ5500E slab gel sequencer (HITACHI).

RESULTS AND DISCUSSION

Pyrene Modification

Cysteine residues in proteins react selectively with *N*-(1-pyrenyl) maleimide. This reaction has been used to quantify cysteine residues in protein.[6] Histone variants do not contain cysteine residues except for the H3 variant. Therefore, point mutation of cysteine for the histone variants enables us to achieve site-specific pyrene modification. We introduced the mutation on the tail domain of H2A to obtain an H2A–H124C or A126C mutant, expecting that photoirradiation against a nucleosome comprised of the pyrene-modified histone and ^{Br}U-substituted DNA would lead to cleavage at the center part of the nucleosome based on MD simulations, which suggested that the domain interacts with the nucleosome dyad.[5] Pyrene modification for H2A mutants was monitored by HPLC. After 3 hours reaction, enhanced UV absorbance was observed close to the unmodified H2A peak (Fig 1a). MALDI-TOF MS analysis revealed that the reaction shifted the molecular weight of H2A by 297.36, which was identical to the molecular weight of *N*-(1-pyrenyl) maleimide (297.31; Fig 1b). Unmodified H2A was also detected in the TOF MS chart even though the sample was purified by HPLC. We did not perform further purification because the retention time of the unmodified and modified H2A were similar, making separation difficult, and the nonmodified H2A would not affect photoreaction in the following experiments. Pyrene modification did not proceed with wild-type H2A. These results suggest that single pyrene modification was successfully performed not at an amino group on the N-terminal but on the substituted cysteine residue.

Nucleosome Reconstitution and UV Irradiation

A nucleosome particle is comprised of two H2A-H2B dimers, one H3-H4 tetramer, and DNA. An H3-H4 tetramer is deposited on DNA to form a tetrasome, subsequently two H2A-H2B dimers are inserted into the tetrasome with the help of histone chaperones in vivo. On the other hand, in vitro nucleosome reconstitution is achieved by removing cation from the mixture of H2A-H2B dimer, H3-H4 tetramer, and DNA. In both cases, a nucleosome in which 146 bp DNA encloses histone octamer is prepared at last. The center part of the nucleosome is called a dyad because it is a symmetry axis of the nucleosome. Size-exclusion chromatography revealed that the pyrene modification on the H2A variant did not affect H2A–H2B heterodimer formation. Nucleosome reconstitution was performed in the presence of 200 nM H2A–H2B dimer and 200 nM H3–H4 tetramer to form 100 nM histone octamer. The inclusion of an excess amount of H3–H4 tetramer helped efficient nucleosome reconstitution. A single nucleosome was required in the subsequent photoirradiation experiment to evaluate nucleosome location.

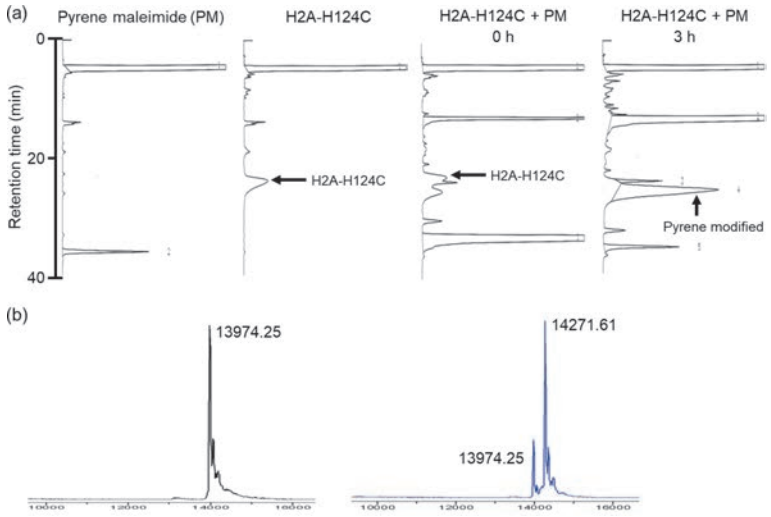

Figure 1. (a) HPLC profiles representing N-(1-pyrenyl) maleimide, unmodified H2A–H124C mutant, the mutant mixed with pyrenyl maleimide, and the mixed sample reacted for 3 hours. Elution was performed with 0.1% TFA containing 5–48% acetonitrile at a flow rate of 3 mL/min at 40 °C. (b) MALDI-TOF MS profiles. Left: the unmodified H2A–H124C mutant. Right: the pyrene-modified mutant.

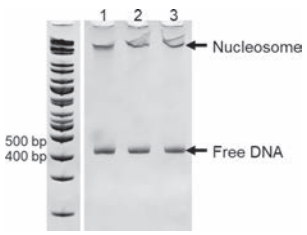

Figure 2. Native PAGE analysis of nucleosome reconstitution. Lanes 1, 2, and 3 represent nucleosomes containing native H2A, pyrene-modified H124C, and pyrene-modified A126C, respectively.

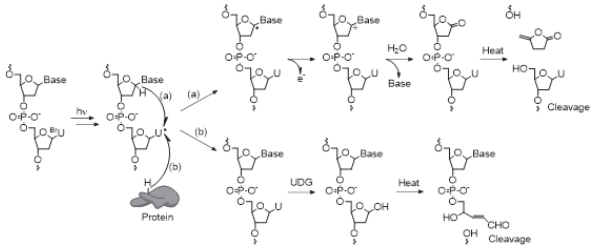

Figure 3. (a) Reaction of uracil radical generated from BrU in the absence of hydrogen donor. (b) Reaction of uracil radical in the presence of protein as hydrogen donor. This case requires uracil DNA glycosylase (UDG) treatment to generate DNA cleavage.

However, the 400 bp DNA fragment was long enough to form a dinucleosome because nucleosome formation requires 146 bp sequences. We applied 0.5 equivalent histone octamer against DNA to inhibit dinucleosome formation, although the reconstitution yield would be less than half. A single-band shift was observed in native PAGE analysis, suggesting that the DNA fragment contained a single nucleosome on the 601 sequence in which the nucleosome formed preferentially.[7] As we expected, the reconstitution ratio yields were less than half and free DNA was observed in the analysis. The yields were identical for native H2A, pyrene-modified H124C, and A126C, suggesting that the modification did not affect nucleosome reconstitution significantly (Fig 2).

It is known that ^{Br}U-substituted DNA is photosensitive and that 302 nm photoirradiation facilitates electron transfer from guanine to ^{Br}U on a specific sequence and generates a uracil radical.[7] The uracil radical abstracts the C1' hydrogen from 2'-deoxynucleotide to generate C1' radical. The radical is oxidized to C1' cation and the cation reacts with H_2O to generate heat-labile 2'-deoxyribonolactone involving the release of base moiety (Fig 3a). In the presence of an excess amount of hydrogen donor including protein, however, most of the uracil radicals are quenched to reduce DNA cleavage efficacy. To recover the efficacy, we treated the irradiated sample with Uracil DNA glycosylase to convert 2'-deoxyuridine generated from uracil radical to heat-labile abasic site so that DNA was cleaved at which electron transfer occurred (Fig 3b).[8]

First, we evaluated the background effect of photoirradiation against a control nucleosome comprised of native histone and ^{Br}U-substituted DNA. No DNA cleavage was observed in slab gel sequencing after 365 nm photoirradiation (Fig 4). However, photoirradiation against the nucleosome comprised of pyrene-modified histone and ^{Br}U-substituted DNA generated two clear DNA cleavage sites (Fig 4). The yield of cleavage reached a plateau at shorter than 20-sec irradiation, confirming the high photosensitivity of pyrene. Although more than half of the DNA was not cleaved at the plateau, considering that the nucleosome reconstitution yields were less than half, most of the ^{Br}U-substituted DNA on nucleosome was cleaved by 20-sec photoirradiation. This timeframe is short enough to allow nucleosome translocation to be analyzed during chromatin dynamics.

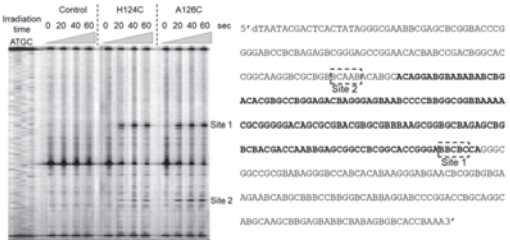

Figure 4. Left: slab gel sequencing analysis of the photoirradiation against nucleosomes containing native H2A (control), pyrene-modified H124C, and pyrene-modified A126C. DNA cleavage sites are denoted as sites 1 and 2. Right: sequence of the DNA fragment containing the 601 sequence which is indicated in bold. The cleavage sites are indicated by dashed rectangles.

As a next step, we located the cleavage sites in the nucleosome. According to MD simulations,[5] the tail domain of H2A, where pyrene modification was introduced, interacts with the dyad part of the nucleosome; therefore, we expected that DNA cleavage would occur at this site (Fig 5a, b). However, the DNA cleavage sites were found at the start and end sites of the 601 sequence in the presence of pyrene-modified H124C and A126C mutant, suggesting that electron transfer from pyrene occurred not at the dyad but at the entry and exit sites of the nucleosome (Fig 5c). These results mean that the tail domain of H2A interacts with the nucleosome entry and exit sites. Given that the histone tail domain is not represented in the crystal structure analysis due to its flexibility.[1] the behavior of this domain remains elusive. Therefore, our novel method is attractive not only for locating nucleosomes, but also for analyzing histone tail domain behavior.

CONCLUSION

In the present work, we developed a novel method exploiting ^{Br}U substitution and pyrene modification to locate nucleosomes using photoirradiation. Site-specific pyrene modification was achieved by cysteine point mutation and reaction with *N*-(1-pyrenyl) maleimide. Photoirradiation against nucleosome comprised of ^{Br}U-substituted DNA and the pyrene-modified histone effectively generated DNA cleavage on the nucleosome entry and exit sites. The method can be used to locate nucleosomes within a short photoirradiation timeframe, which is sufficient to analyze dynamic nucleosome transition. Furthermore, the approach can be useful for analyzing interactions between the histone tail domain and DNA in a nucleosome.

Acknowledgments

We express sincere thanks for a Grant-in-Aid Scientific Research (16H06356 and 20H05936 to H.S.) from Japan Society for the Promotion of Science (JSPS) and NIH award 1R01CA236350 to H.S.

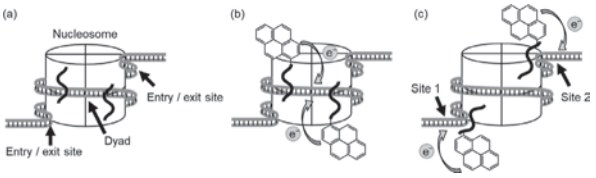

Figure 5. (a) Overview of the nucleosome prepared in the present study. Bold wave lines indicate the tail domain of H2A. (b) The expected electron transfer in which the tail domain interacts with the dyad part of the nucleosome. (c) The suggested electron transfer in which the tail domain interacts with the entry and exit sites of the nucleosome to generate DNA cleavage on sites 1 and 2.

References

1. Luger, K., Maeder, A. W., Richmond, R. K., Sargent, D. F., Richmond, T. J. Crystal structure of the nucleosome core particle at 2.8 Å resolution. *Nature*., 1997; **389**: 251-260.
2. Yang, J. G., Madrid, T. S., Sevastopoulos, E., Narlikar, G. J. The chromatin-remodeling enzyme ACF is an ATP-dependent DNA length sensor that regulates nucleosome spacing. *Nat. Struct. Mol. Biol.*, 2006; **13**: 1078-1083.
3. Yashiro, R., Wang, A. H. J., Sugiyama, H. Photoreactivation of DNA by an Archaeal nucleoprotein Sso7d. *PNAS*, 2006; **103**: 16655-16659.
4. Saha, A., Hashiya, F., Kizaki, S., Asamitsu, S., Hashiya, K., Bando, T., Sugiyama, H. Anovel detection technique of polymerase binding sites by photo-induced electron transfer in ^{Br}U substituted DNA. *Chem. Commun.*, 2015; **51**: 14485-14488.
5. Davey, C. A., Sargent, D. F., Luger, K., Maeder, A. W., Richmond, T. J. Solvent mediated interactions in the structure of nucleosome core particle at 1.9 a resolution. *J. Mol. Biol.*, 2002; **319**: 1097-1113.
6. Winters, R. A., Zukowski, J., Ercal, N., Matthews, R. H., Spitz, D. R. Analysis of glutathione, glutathione disulfide, cysteine, homocysteine, and other biological thiols by high-performance liquid chromatography following derivatization by N-(1-pyrenyl)maleimide. *Anal. Biochem.*, 1995; **227**: 14-21.
7. Watanabe, T., Tashiro, R., Sugiyama, H, Photoreaction at 5'-(G/C)AA^{Br}UT-3' sequence in duplex DNA: Efficient generation of uracil-5-yl radical by charge transfer. *J. Am. Chem. Soc.*, 2007; **129**: 8163-8168.
8. Hashiya, F., Saha, A., Kizaki, S., Li, Y., Sugiyama, H., Locating the uracil-5-yl Radical Formed Upon Photoirradiation of 5- bromouracil-substituted DNA. Nucleic Acids Res., 2014, 42, 13469-13473.

Raman spectra of acetylene-tagged anthraquinone derivatives in various solvents

Hiroki Makanai, Tatsuya Nishihara, and Kazuhito Tanabe*

Department of Chemistry and Biological Science, College of Science and Engineering, Aoyama Gakuin University, 5-10-1 Fuchinobe, Chuo-ku, Sagamihara, Kanagawa 252-5258, Japan

Abstract

We prepared aromatic acetylenes with anthraquinone units and measured their Raman spectra. We identified the robust signal of the acetylene unit at 2200 cm^{-1} upon excitation at 532 nm and noted a significant change in the Raman signal with changing viscosity and polarity of the solvents. Thus, we demonstrate a proof of concept that anthraquinone derivatives can be used as molecular probes for Raman imaging to visualize viscosity or polarity in living cells.

INTRODUCTION

Abnormal changes in intracellular viscosity and polarity are related many disease and malfunction. Thus, monitoring of intracellular viscosity and polarity by molecular probes may be applied to monitor cell status and to understand cellular function. Conventionally, there were various fluorescence probes for measurement of viscosity and polarity in the cells.[1,2] However, fluorescence probes have some drawbacks such as photobleaching of the fluorophores and requirement of large molecules for easily viewable imaging. Therefore, to complement the missing part of fluorescence probes, another technology to visualize viscosity and polarity has been required.

Raman spectroscopy has been well-documented as a potent technology for visualization of biomolecules in cells and tissues.[3,4] This method has been utilized to identify specific vibrational signals of molecules and to provide a fingerprint for identification. Thus, measurement of Raman spectra is important for extended analysis of molecular behavior and their environment. Recently, various alkyne-tagged small probes have been applied to biological imaging of cellular organelles such as cell nuclei[5] and mitochondria.[6,7] Our group also reported that the hypoxic region in cells could be visualized using a nitroimidazole derivative.[8] The small acetylene unit shows a typical Raman signal around 2100-2200 cm^{-1}, at which inherent cellular background signals were negligible. Thus, acetylene-tagged compounds are expected to act as molecular probes for biological factors and environments.

Herein, we found that the Raman spectra of acetylene-tagged aromatic compounds in several solvents were able to use for monitoring of the local environments in biological systems. We employed 2-ethynyl anthraquinone derivatives as candidate molecules because of their strong signal around 2100-2200 cm^{-1} attributed to the aromatic acetylene. We prepared AQ-PhNH_2 and AQ-Ph (Scheme 1), and measured their Raman spectra. We found that both molecules showed typical signal around 2200 cm^{-1} attributed to the acetylene unit. In addition, we confirmed that AQ-PhNH_2 showed a solvent-dependent change of the signal. AQ-PhNH_2 is expected to enable us to monitor the polarity or viscosity around the molecules in biological systems.

MATERIALS AND METHODs

General Method. Reagents were purchased from Wako pure chemical industries, Tokyo chemical industries and Sigma Aldrich. AQ-Ph was synthesized by the methods reported previously.[9] NMR spectra were recorded on JEOL JIN-ECX500 II (^{1}H:500 MHz,^{13}C:125 MHz) spectrometer and chemical shifts were expressed in ppm downfield from tetramethylsilane, using residual protons in solvents as internal standards (dimethyl sulfoxide-d_6 :δ = 2.50). UV-visible spectra were obtained at 200-700 nm using a JASCO V-630 UV/VIS spectrophotometer. Raman spectrum measurement was carried out on a RENISHAW in Via Raman Microscope.

Synthesis of AQ-PhNH_2. Copper (I) iodide (18 mg, 94.7 μmol) and tetrakis (triphenylphosphine) palladium (0) (131 mg, 113 μmol) were added to a mixture of 4-ethynylaniline (384 mg), 2-bromoanthoraquinone (669 mg, 2.33 mmol) in triethylamine (3 mL, 22 mmol) and DMF (6 mL), and the resulting mixture was stirred at 90 ˚C for 30 min. After the reaction, the mixture was extracted with EtOAc and water, and the organic layer was dried over $MgSO_4$ and concentrated at reduced pressure. The crude product was purified by silica gel column chromatography (hexane/ethyl acetate = 1:1) to give AQ-PhNH2 (710mg, 94 %) as a red solid; MP. >300 ˚C; ^{1}H NMR (DMSO-d_6, 500 MHz) δ 8.23–8.20 (m, 2H), 8.19 (d, J = 8 Hz, 1H), 7.95–7.93 (m, 2H), 7.92 (d, J = 1.5 Hz, 1H), 7.37–7.40 (m, 3H), 7.30 (d, J = 8.5 Hz, 2H), 6.58 (d, J = 8.5 Hz, 2H), 5.76 (s, 2H); ^{13}C NMR (125 MHz, DMSO-d_6) δ182.6, 182.2, 151.0, 136,2 135.2, 135.0, 134.1, 133.8, 133.7, 133.5, 132.0, 130.2, 129.2, 128.8, 127.8, 127.3, 114.2, 114.1, 97.7, 86.6 FABMS (NBA) *m/z* 323 [(M + H)$^+$]; HRMS calcd. for $C_{22}H_{13}NO_2$ [(M + H)$^+$] 323.0946, found 323.0944.

Measurement of Raman Spectra of Anthraquinone Derivatives. Anthraquinone derivatives were solved in designated solvents and measured their Raman spectra (Ex. 532 nm).

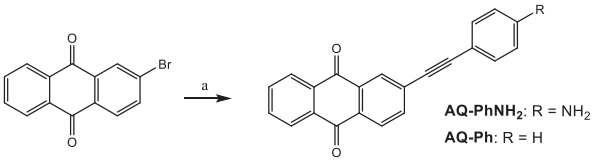

Scheme 1. Reagents and conditions. (a) 4-ethynylaniline (for AQ-PhNH$_2$) or ethynylbenzene (for AQ-Ph), Et_3N, $Pd(PPh_3)_4$, CuI, DMF, 94% (for AQ-PhNH$_2$) or 47% (for AQ-Ph).

RESULTS AND DISCUSSION

AQ-PhNH$_2$ was prepared by coupling of bromoanthraquinone and ethynylaniline phenylacetylene (Scheme 1). Initially, we measured the Raman spectra of AQ-PhNH$_2$ with 532 nm excitation under various conditions. As shown in Fig. 1A, AQ-PhNH$_2$ in dioxane showed a strong signal at 2211 cm^{-1} arising from the acetylene group. By contrast, the changing the solvent from dioxane resulted in a significant change in Raman spectra. Solubilization in a polar solvent such as pyridine or DMF led to the appearance of a shoulder band at a lower wavenumber, and solubilization in DMSO resulted in the strongest signal at 2191 cm^{-1}. We also measured the Raman spectra of AQ-PhNH$_2$ in MeOH containing glycerol (Fig. 1B). These two solvents show similar polarities, but their viscosities differ. The AQ-PhNH$_2$ showed a signal typical of the acetylene unit in MeOH. It is striking that increasing viscosity with an increase in glycerol content resulted in an enhancement of the signal at 2191 cm^{-1}. These results strongly indicate that the signal of the acetylene unit in AQ-PhNH$_2$ was affected by the surrounding environment, and that the wavenumber of the acetylene unit can be an indicator for the polarity or viscosity.

In a separate experiment, we prepared a control compound, AQ-Ph, and characterized its Raman spectra to confirm whether there was a relationship between chemical structure and function. The synthesis of AQ-Ph was conducted as described for AQ-PhNH$_2$. As shown in Figure 2, a limited change of Raman band of its acetylene unit was observed in both polar solvents and glycerol-containing solvents. Thus, the amino group on the phenyl ring in anthraquinone is responsible for the signal change in various solvents.

Further, we measured Raman spectra of AQ-PhNH$_2$ in D-MEM (Dulbecco's Modified Eagle Medium)-containing solution in order to evaluate the function of probe under the conditions which mimicked the biological environments. As illustrated in Fig. 3, AQ-PhNH$_2$ showed the formation of the signal at 2191cm^{-1} under the viscous media with DMEM, while AQ-PhNH$_2$ in the non-viscous solvent with DMEM did not show the signal at 2191cm^{-1}, suggesting that AQ-PhNH$_2$ acts as molecular probe in the biological environments.

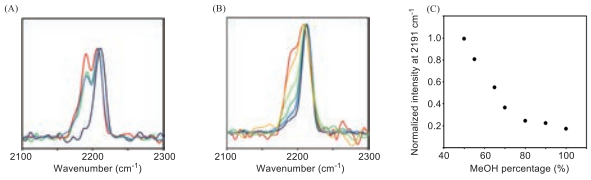

Figure 1. (A) Raman spectra of AQ-PhNH$_2$ (1 mM) in dioxane (dark blue), pyridine (blue), DMF (green) and DMSO (red). (B) Raman spectra of AQ-PhNH$_2$ (1 mM) in MeOH-glycerol (100% MeOH: dark blue, 90% MeOH: blue, 80% MeOH: light blue, 70% MeOH: green, 65% MeOH: light green, 55% MeOH: orange, 50% MeOH: red). (C) Plot of signal intensity against MeOH percentage (viscosity). The intensity was obtained from Figure 1B.

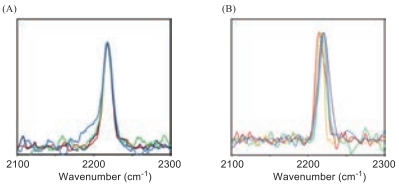

Figure 2. (A) Raman spectra of AQ-Ph (1 mM) in dioxane (dark blue), pyridine (blue), DMF (green) and DMSO (red). (B) Raman spectra of AQ-Ph (1 mM) in MeOH-glycerol (100% MeOH: dark blue, 90% MeOH: blue, 80% MeOH: light blue, 70% MeOH: green, 55% MeOH: orange, 50% MeOH: red).

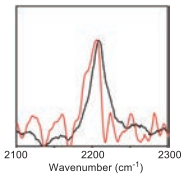

Figure 3. Raman spectra of AQ-PhNH$_2$ (1 mM) in MeOH-glycerol (50% Glycerol + 40% MeOH + 10% DMEM: red, 0% glycerol + 90% MeOH + 10% DMEM: black).

CONCLUSION

We have synthesized anthraquinone derivatives bearing a phenylacetylene unit and measured their Raman spectra. The AQ-PhNH$_2$ with aminophenyl group at the 2-position showed the expected strong signal of the acetylene group at 2211 cm^{-1}, which shifted to 2191 cm^{-1} in high polar or viscous solvents. The control compound, AQ-Ph, showed a moderate signal shift even in these solvents; thus, the amino group is a key substituent for this signal change. The sensitive change observed in Raman signal provides a means of detecting the environmental changes in a biological system.

The molecules prepared in this study are potent probes to monitor cellular viscosity and polarity. But, it is difficult to distinguish between changes in cell polarity and viscosity by the present probes. Preparing the improved probes which respond only to viscosity or polarity is in progress.

REFERENCES

(1) Li, M., Fan, J., Li, H., Du, J., Long, S., Peng, X. A ratiometric fluorescence probe for lysosomal polarity. *Biomaterials*, **2018**, *164*, 98-105.

(2) Gupta, N., Reja, S. I., Bhalla, V., Gupta, M., Kaur, G., Kumar, M. A bodipy based fluorescent probe for evaluating and identifying cancer, normal and apoptotic C6 cells on the basis of changes in intracellular viscosity. *J. Mater. Chem. B*, **2016**, *4*, 1968-1977.

(3) Antonio, K. A., Schultz, Z. D. Advances in biomedical Raman microscopy. *Anal. Chem.*, **2014**, *86*, 30-46.

(4) Huser, T., Chan, J. Raman spectroscopy for physiological investigations of tissues and cells. A*dv. Drug Deliv. Rev.* **2015**, *89*, 57-70.

(5) Yamakoshi, H., Dodo, K., Okada, M., Ando, J., Palonpon, A., Fujita, K., Kawata, S., Sodeoka, M. Imaging of EdU, an Alkyne-tagged cell proliferation probe, by Raman microscopy. *J. Am. Chem. Soc.*, **2011**, *133*, 6102-6105.

(6) Yamakoshi, H., Palonpon, A., Dodo, K., Ando, J., Sawata, S., Fujita, K., Sodeoka, M. A sensitive and specific Raman probe based on bisarylbutadiyne for live cell imaging of mitochondria. *Bioorg. Med. Chem. Lett.*, **2015**, *25*, 664-667.

(7) Li, Y., Heo, J., Lim, C. -K., Pliss, A., Kachynski, A. V., Kuzmin, A. N., Kim, S., Prasad, P. N. Organelle specific imaging in live cells and immuno-labeling using resonance Raman probe. *Biomaterials*, **2015**, *53*, 25-31.

(8) Kurihara, R., Ikemura, Y., Tanabe, K. Preparation of alkyne-labeled 2-nitroimidazoles for identification of tumor hypoxia by Raman spectroscopy. *Bioorg. Med. Chem. Lett.*, **2016**, *26*, 4892-4894.

(9) Vasilevsky, S. F, Davydowa, M. P., Mamatuk, V. I., Tsvetkov, N., Hughes, A., Baranov, D. S., Alabugin, I. V. Full cleavage of C≡C bond in electron-deficient alkynes via reaction with ethylenediamine. *Aust. J. Chem.*, **2017**, *70*, 421-429.